Volume 10 | Number 32 | 28 August 2019 | Pages 7475–7660

Chemical Science

rsc.li/chemical-science

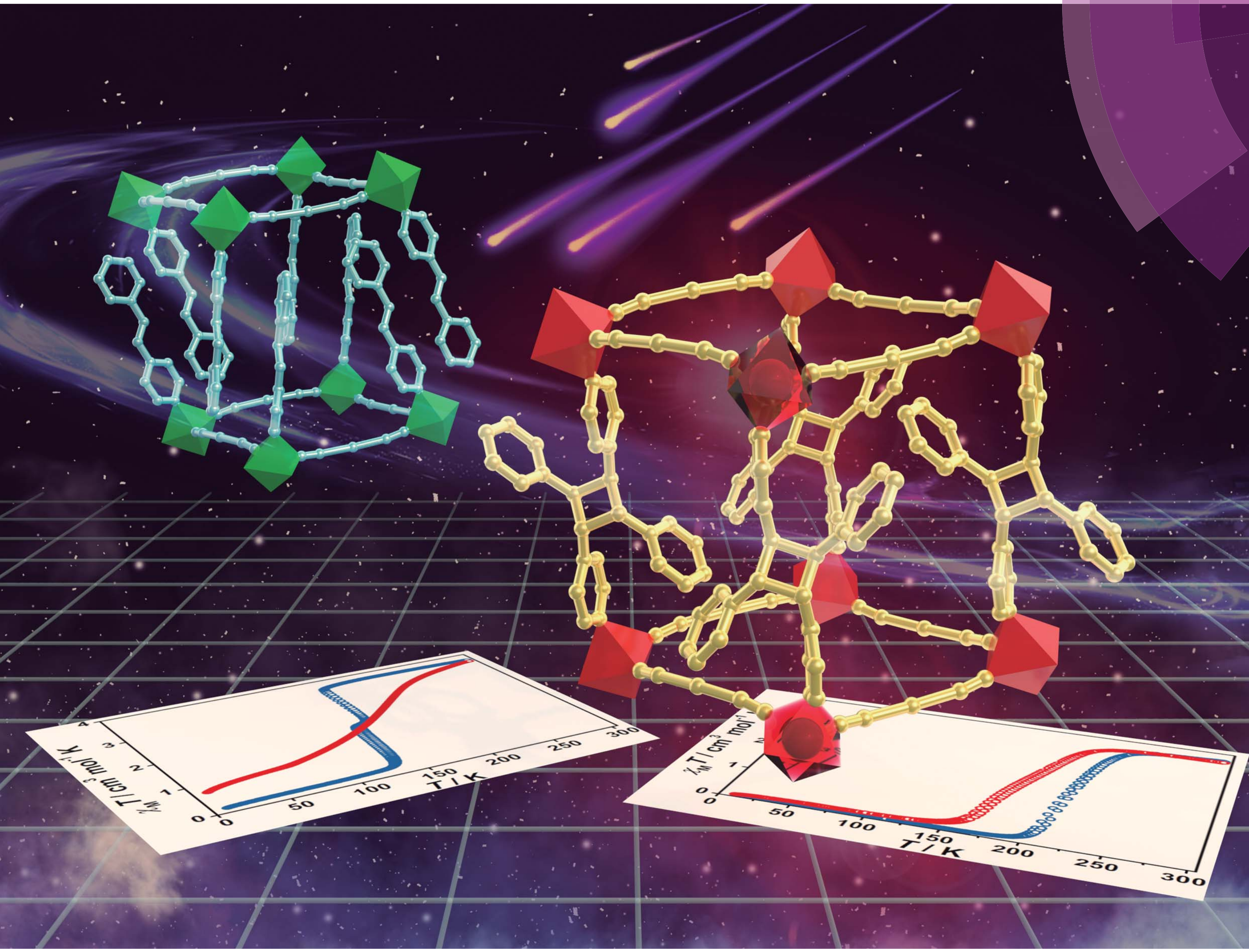

ISSN 2041-6539

ROYAL SOCIETY OF CHEMISTRY | Celebrating IYPT 2019

EDGE ARTICLE
Ming-Liang Tong *et al.*
Spin-crossover modulation *via* single-crystal to single-crystal photochemical [2 + 2] reaction in Hofmann-type frameworks

Chemical Science

EDGE ARTICLE

View Article Online
View Journal | View Issue

Check for updates

Cite this: *Chem. Sci.*, 2019, **10**, 7496

All publication charges for this article have been paid for by the Royal Society of Chemistry

Spin-crossover modulation *via* single-crystal to single-crystal photochemical [2 + 2] reaction in Hofmann-type frameworks†

Long-Fei Wang, Wei-Man Zhuang, Guo-Zhang Huang, Yan-Cong Chen, Jiang-Zhen Qiu, Zhao-Ping Ni and Ming-Liang Tong*

Received 9th May 2019
Accepted 3rd July 2019

DOI: 10.1039/c9sc02274k

rsc.li/chemical-science

This study reports the first modulation of spin-crossover (SCO) behavior *via* a photochemical [2 + 2] cycloaddition reaction. Here we construct two no-solvent Fe(II)–Ag(I) bimetallic Hofmann-type frameworks, $[Fe(4\text{-spy})_2\{Ag(CN)_2\}_2]$ (**1**) and $[Fe(2,4\text{-bpe})_2\{Ag(CN)_2\}_2]$ (**2**) (4-spy = 4-styrylpyridine, 2,4-bpe = *trans*-1-(2-pyridyl)-2-(4-pyridyl)ethylene). For **1**, the dimerization of 4-spy results in a single-crystal to single-crystal (SCSC) transformation from 2D interdigitated layers to a 3D interpenetrated structure. Additionally, a 3D → 3D structural transformation accompanied with Ag(I)–N bond breaking is achieved *via* the photochemical cycloaddition reaction of 2,4-bpe in **2**. More importantly, both the spin transition temperatures and the SCO character are effectively modulated; thus, this approach provides a new strategy for constructing photo-responsive SCO magnetic materials.

Introduction

Scientists have focused on making advanced materials with functionalities that respond to external stimuli.[1] A promising method that has been rapidly developed is the post-synthetic modification (PSM) of coordination polymers.[2–5] One particularly interesting type of PSM is the single-crystal to single-crystal (SCSC) structural transformation *via* a photochemical [2 + 2] cycloaddition reaction.[6–11] The stereoselective photodimerization of olefins can proceed in the solid-state if the reactive C═C bonds are parallel and separated by less than 4.2 Å.[12,13] This results in the modulation of physical properties, such as magnetism,[14–17] photoluminescence,[18] and conductivity,[19,20] which has been previously reported.

Spin-crossover (SCO) compounds are fascinating advanced materials that can switch between high-spin (HS) and low-spin (LS) states under external stimuli (temperature, light, or pressure).[21,22] More importantly, the population of SCO behavior in crystal lattice is highly dependent on the presenting elastic cooperativity between metal centers.[23] As a result, slight structural perturbations, such as π-stacking, hydrogen bonding and van der Waals contacts, in the crystal lattice can significantly affect the cooperativity of SCO behavior such as abruptness, hysteresis and steps. For example, SCO properties are highly sensitive to anions, solvents or guests.[24–26] As a result, porous SCO metal–organic frameworks (MOFs) have been actively explored. Their SCO behaviors can be adjusted by guest adsorption and desorption.[27–32] Moreover, successful covalent PSMs have been obtained through chemical reaction of an active guest,[33] redox intercalation of a coordinatively unsaturated metal site,[34,35] and chemical modification of a bridging ligand.[36] However, the unreacted chemical reagents and solvents left in the pores can also affect SCO properties, which hinders the analysis on the modulation mechanism. PSM within the framework itself, without introducing other reagents, can prevent this problem. For example, some photochromic building units have been introduced into SCO systems to develop novel photo-responsive magnetic materials,[37,38] such as the *cis*–*trans* photoisomerization of stilbenes[39–41] or azobenzenes,[42] and the intramolecular photocyclization of dithienylethene.[43–46] The photochemical [2 + 2] cycloaddition reaction, which can induce drastic changes of structural dimensionality, the electronic conjugation and the supramolecular interaction, shall shows promising impacts on the SCO properties, but such challenging integration has not been reported.

In the present study, a regioselective photochemical [2 + 2] cycloaddition reaction was incorporated into the SCO framework for the first time (Scheme 1). After UV irradiation, two solvent-free SCO frameworks, $[Fe(4\text{-spy})_2\{Ag(CN)_2\}_2]$ (**1**, 4-spy = 4-styrylpyridine) and $[Fe(2,4\text{-bpe})_2\{Ag(CN)_2\}_2]$ (**2**, 2,4-bpe = *trans*-1-(2-pyridyl)-2-(4-pyridyl)ethylene), undergo quantitative SCSC photodimerization to produce $[Fe(\textit{rctt}\text{-4-ppcb})\{Ag(CN)_2\}_2]$ (**1′**, *rctt*-4-ppcb = *rctt*-1,3-bis(4-pyridyl)-2,4-bis(phenyl)cyclobutane, *r* = reference group, *c* = cis and *t* =

Key Laboratory of Bioinorganic and Synthetic Chemistry of Ministry of Education, School of ChemistrySun, Yat-Sen University, Guangzhou, 510275 P. R. China. E-mail: tongml@mail.sysu.edu.cn; Fax: +86 20 8411 2245

† Electronic supplementary information (ESI) available. CCDC 1897816–1897818, 1897822–1897824, 1897819–1897821 and 1897825–1897827. For ESI and crystallographic data in CIF or other electronic format see DOI: 10.1039/c9sc02274k

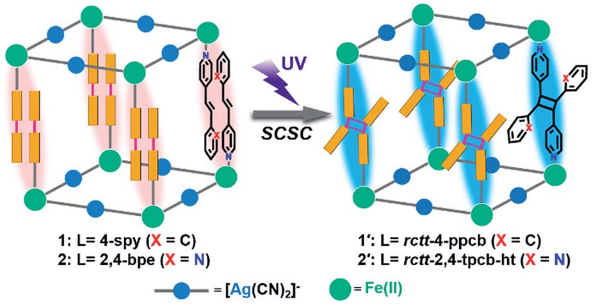

Scheme 1 Strategy for the incorporation of a photochemical [2 + 2] cycloaddition into SCO Hofmann-type frameworks [Fe(L)$_2${Ag(CN)$_2$}$_2$].

trans) and [Fe(*rctt*-2,4-tpcb-ht){Ag(CN)$_2$}$_2$] (**2′**, *rctt*-2,4-tpcb-ht = *rctt*-1,3-bis(2-pyridyl)-2,4-bis(4-pyridyl)cyclobutane, ht = head-to-tail). A comprehensive study and discussion on the variations of structures and magnetic dynamics convincingly demonstrate the effectiveness of photochemical [2 + 2] reaction on tuning spin crossover magnetic responses.

Results and discussion

Compound **1** was obtained as orange block singe crystals through the slow diffusion of Fe(ClO$_4$)$_2$·6H$_2$O, KAg(CN)$_2$ and 4-spy ligand in EtOH solution. Replacing of 4-spy by 2,4-bpe ligand in the similar synthetic route gave the block single crystals of **2** with deeper color. Magnetic susceptibility measurements reveal hysteretic one-step and two-step SCO behaviors for **1** and **2**, respectively (Fig. 1). For **1**, $\chi_M T$ values decrease gradually from 3.71 cm^3 mol^{-1} K^{-1} at 300 K to 3.61 cm^3 mol^{-1} K^{-1} at 250 K then decrease suddenly to 0.10 cm^3 mol^{-1} K^{-1} at 180 K, indicating a complete SCO behavior (Fig. 1a and S1a†). The critical temperatures in the cooling and warming modes are 212 and 215 K (Table S1†), respectively, revealing a 3 K thermal hysteresis loop. Such hysteretic SCO property is further confirmed by the differential scanning calorimetry (DSC) measurement with exothermic and endothermic peaks at 207 and 210 K, respectively (Fig. S2a†). For **2**, obvious plateaus are observed in the range of 149–158 K (cooling mode) and 153–160 K (warming mode) (Fig. 1b and S3a†), corresponding to the HS$_{0.5}$LS$_{0.5}$ state. The critical temperatures are $T_{c1}\downarrow$ = 164 K, $T_{c1}\uparrow$ = 167 K, $T_{c2}\downarrow$ = 141 K and $T_{c2}\uparrow$ = 146 K, defining 3 and 5 K thermal hysteresis loops, respectively (Table S1†). Furthermore, DSC measurements (Fig. S4†) reveal peaks at $T_{c1}\downarrow$ = 161 K, $T_{c1}\uparrow$ = 166 K and $T_{c2}\downarrow$ = 138 K, $T_{c2}\uparrow$ = 146 K, which are consistent with the T_c values from the magnetic data.

Variable-temperature single-crystal X-ray diffraction data were collected at 120, 212, and 260 K for **1** and 120, 155, and 185 K for **2** (Tables S3 and S4†). Compound **1** remains in the orthorhombic space group *Pbac*, and all the Fe(II) ions are crystallographically equivalent at all the measured temperatures. The average distance of Fe–N bond contracts from 2.157 Å at 260 K to 1.956 Å at 120 K (Table S5†), corresponding to a complete interconversion between HS and LS of the Fe(II) ions and matches well with the magnetic data. The structure at 260 K is described representatively in the following. Its asymmetric unit contains a half-occupied Fe(II) ion located at the inversion center, one [Ag(CN)$_2$]$^-$ ion and one 4-spy ligand (Fig. S5a†). The octahedral Fe(II) ions are bridged equatorially by four separate [Ag(CN)$_2$]$^-$ linkers to form rhombic [Fe$_4${Ag(CN)$_2$}$_4$] grids and then generate corrugated 2D [Fe{Ag(CN)$_2$}$_2$]$_\infty$ layers (Fig. 2a). Each Fe(II) ion is coordinated axially by two monodentate 4-spy ligands, resulting in a 2D Hofmann-type coordination polymer (Fig. 2d). The 4-spy ligands are disordered in two positions with a ratio of 66 : 34, suggesting the pendulum movement of the benzene rings.

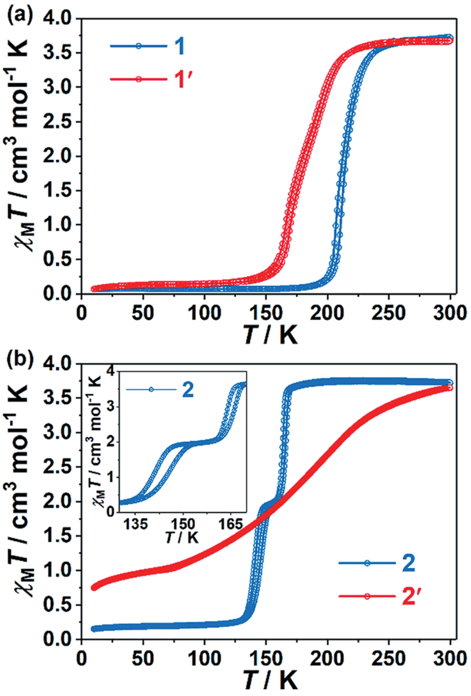

Fig. 1 Magnetic susceptibility data for **1** (a, blue) and **2** (b, blue) and their photochemical [2 + 2] cycloaddition products **1′** (a, red) and **2′** (b, red).

Moreover, it should be noted each [Fe$_4${Ag(CN)$_2$}$_4$] grid in the 2D layer possesses a rhombic window and is further threaded by two 4-spy ligands from adjacent upper and lower layers, respectively, giving the interdigitation of layers (Fig. S6a–d†). The shortest interlayer Ag(I)···Ag(I) distance is 7.40 Å, indicating the absent of argyrophilic interaction which is usually observed in 2D or 3D Hofmann-type SCO compounds. Offset face-to-face π···π interactions are observed between the benzene and pyridine rings, with dihedral angles of 13.6° and 9.2° for the two disordered ligands and a centroid-to-centroid distance of 4.01 Å at 260 K (Fig. S7a and Table S6†). Most importantly, the center-to-center distances between the parallel ethylene groups of the two disordered 4-spy ligands are 3.97 and 3.84 Å, which satisfies Schmidt's photochemical [2 + 2] cycloaddition reaction criteria (<4.2 Å).[12,13]

Compound **2** crystalizes in the monoclinic space group *P*2$_1$/*c*, and only one crystallographically independent Fe(II) ion is observed at 120 and 185 K. The coordination environment around the Fe(II) ion is similar to that in **1** (Fig. S8a†). Instead of 4-spy in **1**, the 4-pyridyl unit of 2,4-bpe ligand is axially

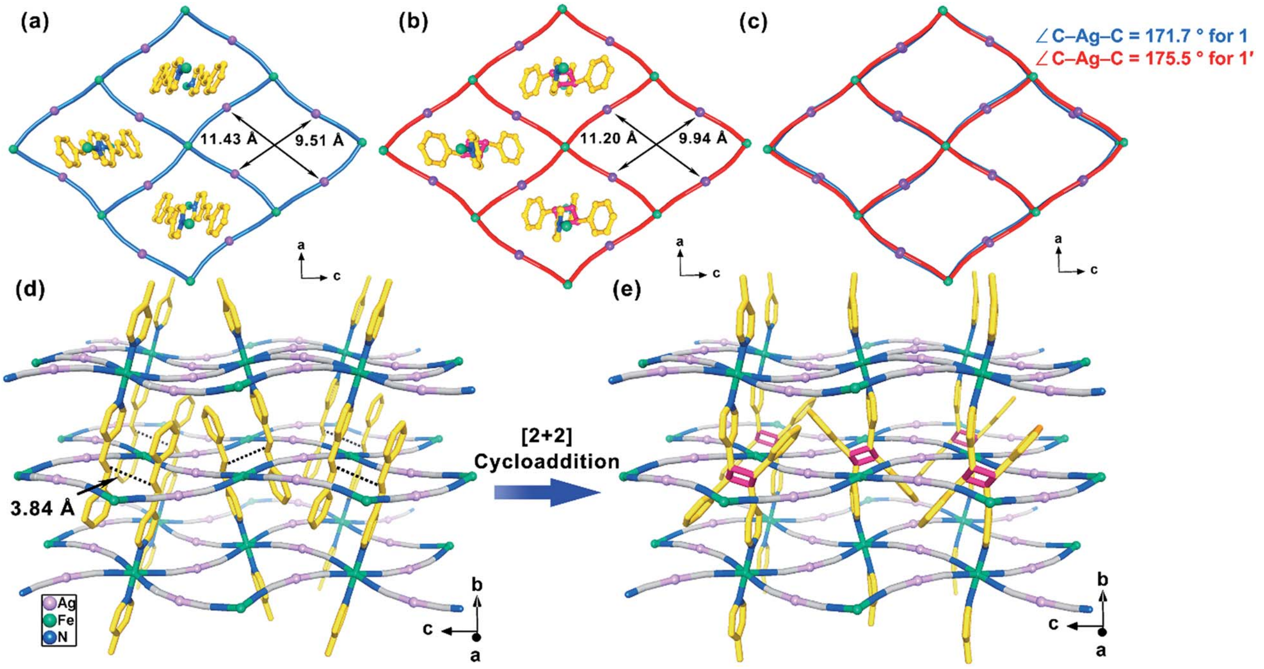

Fig. 2 The $[Fe\{Ag(CN)_2\}_2]_\infty$ layer of **1** (a) and **1′** (b). An overlap between $[Fe\{Ag(CN)_2\}_2]_\infty$ layers of **1** (blue) and **1′** (red) (c) at 260 K indicates the slight structural reorganization of $[Fe_4\{Ag(CN)_2\}_4]$ grids. A view shows structural changes from 2D interdigitated layers of **1** (d) to the 3D interpenetrated structure of **1′** (e). The organic ligands in the middle layers are omitted for clarity. The distance between the center of C═C group are labeled and represented as black dashed lines.

coordinated to the Fe(II) ion in **2**. The average Fe–N distances (Table S7†) are 1.967 Å (120 K) and 2.174 Å (185 K), corresponding to the LS and HS states, respectively. Moreover, each $[Fe_4\{Ag(CN)_2\}_4]$ grid is threaded by two 2,4-bpe ligands from neighboring layers with offset π⋯π interactions between the pyridine rings (Fig. S9a†). The distance between the centers of the C═C groups of the 2,4-bpe ligands is 3.91 Å at 185 K, indicating the possibility of photo-dimerization reaction. Notably, the 2-pyridyl groups of the two trapped 2,4-bpe ligands further coordinate to Ag(I) ions on the opposite edges of the $[Fe_4\{Ag(CN)_2\}_4]$ grid (Fig. 3a), generating a unique 3D Hofmann-type coordination polymer (Fig. 3d). A topological analysis with TOPOS 4.0 (ref. 47 and 48) yields a (3,6)-connected *rtl* topological net (Fig. S10†). Due to the additional Ag(I)–N_{py} bond, the 2,4-bpe ligand is fixed, and no structural pendulum movement is observed. Moreover, the $Ag(CN)_2^-$ unit with a C–Ag(I)–C angle of 158.2(3)° in **2** at 185 K is more bent[49] than that in **1**. When the temperature decreases from 185 to 155 K, symmetry breaking from $P2_1/c$ to $P\bar{1}$ is observed (Table S4†), together with a conversion from one to two crystallographically independent Fe(II) ions (Fig. S11 and S12†). The average Fe–N distances of the Fe1 and Fe2 ions are 1.960 and 2.165 Å, respectively, which is in good agreement with the intermediate $HS_{0.5}LS_{0.5}$ state observed in the magnetic data.

Photochemical [2 + 2] cycloaddition reactions were performed by irradiating single crystals of **1** and **2** for three and four days, respectively, under an high-pressure mercury lamp (P = 500 W), which quantitatively yielded the photoproducts **1′** and **2′**, respectively, *via* a SCSC transformation. The single crystals of **1** remained intact during the whole irradiation process. The photochemical reaction process can be directly monitored *via* the crystal color change from orange to light gray (Fig. 4a). In contrast, the single crystals of **2** are cracked into pieces with color change from orange to light gray (Fig. S13†) after 4 days, in which some pieces still keep the single crystal properties. In consistent with the observed photochromic effect of the crystals after irradiation, both photoproducts show the obvious decrease of absorption in the visible region (Fig. S14†).

Further ^1H NMR spectra measurement of the digestion products of **1′** and **2′** in D_6-DMSO reveal 99% and 95% conversions of the 4-spy ligands to *rctt*-4-ppcb and the 2,4-bpe ligands to *rctt*-2,4-tpcb-ht. The signal at 4.60 ppm corresponds to the C–H protons of the cyclobutane ring in *rctt*-4-ppcb (Fig. 5). Meanwhile, the signals at 4.78 and 4.84 ppm are the characteristic signals of the cyclobutane protons of *rctt*-2,4-tpcb-ht, indicating a regioselective ht [2 + 2] photocycloaddition (Fig. S15†). The IR spectra (Fig. S16†) also show the disappearance of the C═C–H out-of-plane bending vibrations at 967 cm^{-1} (978 cm^{-1}) for **1** (**2**) and appearance of the saturated C–H stretching vibrations at 2934 cm^{-1} (2928 cm^{-1}) for **1′** (**2′**), respectively. The PSM processes are further supported by the powder X-ray diffraction patterns (Fig. S17 and S18†). To the best of our knowledge, a photochemical [2 + 2] cycloaddition reaction based on an Fe(II) coordination compound has not been previously reported.

The regioselective [2 + 2] photocycloaddition is clearly confirmed by the single-crystal analysis (at 120, 178, and 260 K for **1′** and 90, 185, and 300 K for **2′**). After the UV irradiation of **1**, the space group *Pbac* is retained with comparable unit cell dimensions. The main change is that the two 4-spy ligands trapped in each $[Fe_4\{Ag(CN)_2\}_4]$ grid are dimerized to form a bis-monodentate *rctt*-4-ppcb ligand, which bridges the upper and

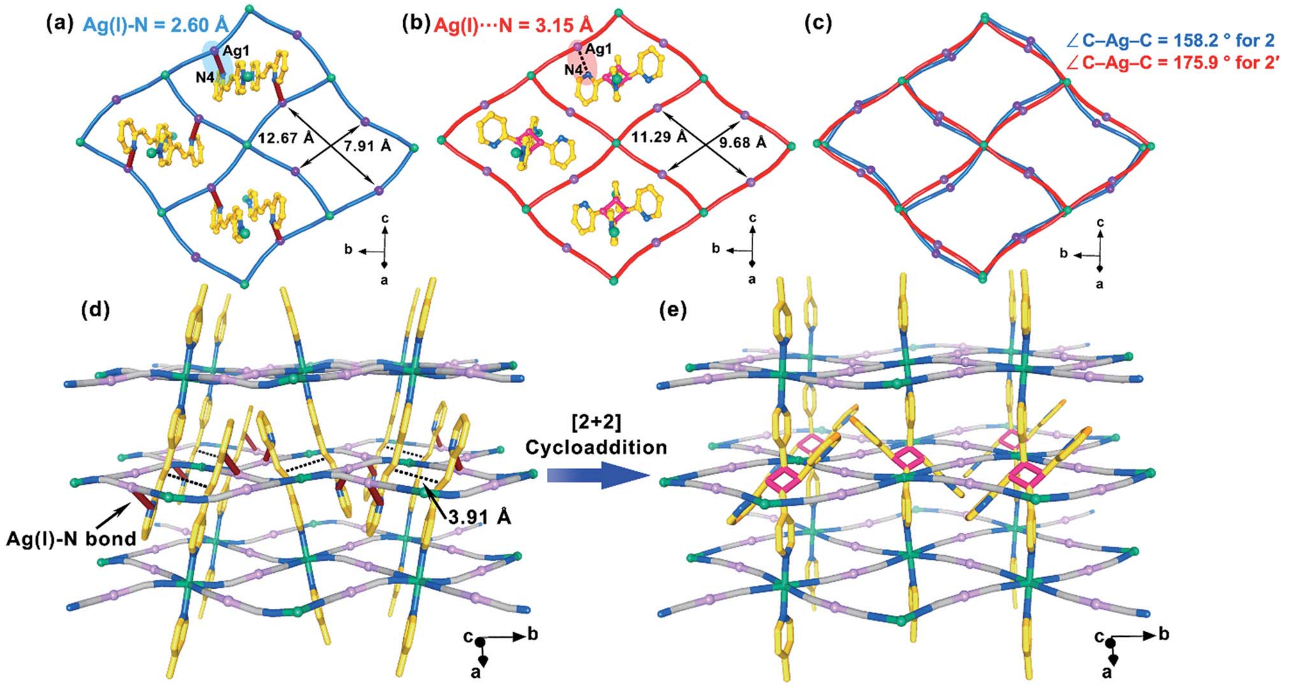

Fig. 3 The $[Fe\{Ag(CN)_2\}_2]_\infty$ layer of **2** (a) and **2′** (b). An overlap between $[Fe\{Ag(CN)_2\}_2]_\infty$ layers of **2** (blue) and **2′** (red) (c) indicates the drastic structural reorganization of $[Fe_4\{Ag(CN)_2\}_4]$ grids. A view shows the structural changes from 3D *rtl*-type structure of **2** (d) to the 3D interpenetrated structure of **2′** (e). The organic ligands in the middle layers are omitted for clarity. The Ag(I)–N_{py} bonds rings in **2** are highlighted as brown rods. The distance between the center of C=C group are labeled and represented as black dashed lines.

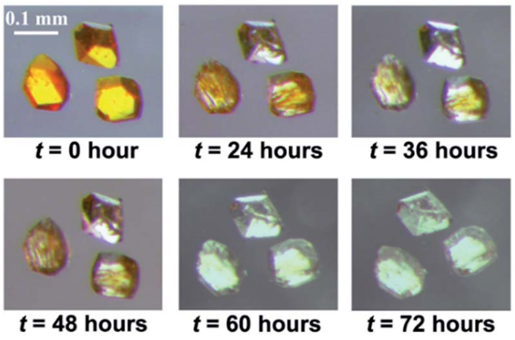

t = 0 hour *t* = 24 hours *t* = 36 hours

t = 48 hours *t* = 60 hours *t* = 72 hours

Fig. 4 Single crystal pictures of **1** under the exposure of high-pressure Hg lamp (*P* = 500 W) at different irradiation times, showing obvious color change from orange to light gray.

lower layers to form a twofold-interpenetrated 3D framework with *pcu* topology (Fig. 2e and S6e–h†). Therefore, a 2D → 3D SCSC photochemical transformation has been achieved. Accordingly, due to the geometric restrictions of the cyclobutane ring with sp^3 hybridization, the dihedral angle between the benzene and the pyridine rings changes from 13.6° to 41.5° at 260 K (Table S6†). Meanwhile, offset face-to-face π···π interactions between the trapped 4-spy ligands in **1** are replaced by edge-to-face π···π interactions between the intermolecular *rctt*-ht substituted cyclobutanes in **1′** (Fig. S7b†). The comparison of 2D fingerprint plots between **1** and **1′** further confirm the different supramolecular interaction (Fig. 6).[50] Obviously, as revealed by the 2D fingerprint plots of C···C contacts, the blue region around $d_e \approx d_i \approx 1.8$ Å in **1** (Fig. 6a) is absent in **1′** (Fig. 6c), corresponding to the losing of π···π stacking between the aromatic rings.[51] Meanwhile, the positions of the 'wings' in the fingerprint plots, which correspond to C–H···π interactions become more visually dominant in **1′**(Fig. 6b) than **1** (Fig. 6d), suggesting an additional contribution from edge-to-face π···π interactions.

A regiospecific [2 + 2] photodimerization is also achieved during the **2** → **2′** process, which forms the *rctt*-2,4-tpcb-ht link. Interestingly, the Ag(I)–N_{py} bond between the Ag(I) ion and the 2-pyridyl unit in **2** is broken in **2′** (Ag···N = 3.15 Å at 300 K) (Fig. 3b), which should be resulted from the geometric restriction of *rctt*-2,4-tpcb-ht ligand. Moreover, it is found the pyridine rings of the bridging ligand is disordered with a 50 : 50 ratio (Fig. S8b†). Similar to *rctt*-4-ppcb ligand in **1′**, the dihedral angles between two adjacent pyridine units are changed to 46.9 and 45.1° at 300 K for two disordered parts (Table S6†), leading to edge-to-face π···π interactions between *rctt*-4-ppcb ligand (Fig. S9b†). Thus, a twofold-interpenetrated 3D framework with a *pcu* net is also formed in **2′** (Fig. S10e–h†). As far as we know, this represents the first example of a 3D → 3D SCSC photochemical transformation associated with bond breaking.

Magnetic susceptibility measurements reveal that the SCO behaviors are dramatically modulated by the photochemical [2 + 2] cycloaddition reaction. The spin transition curve of **1′** is more gradual and occurs at a lower temperature compared to that of **1** (Fig. 1a). In contrast to the one-step hysteresis of **1**, two-step hysteretic SCO ($T_{c1}\downarrow$ = 190 K, $T_{c1}\uparrow$ = 194 K, $T_{c2}\downarrow$ = 166 K and $T_{c2}\uparrow$ = 169 K) without an obvious plateau is observed in **1′**. This is further confirmed by the DSC measurements ($T_{c1}\downarrow$ = 193 K, $T_{c1}\uparrow$ = 198 K, $T_{c2}\downarrow$ = 165 K and $T_{c2}\uparrow$ = 167 K, Fig. S2b†). For **2′**, an incomplete, gradual and one-step SCO (T_c = 162 K) without

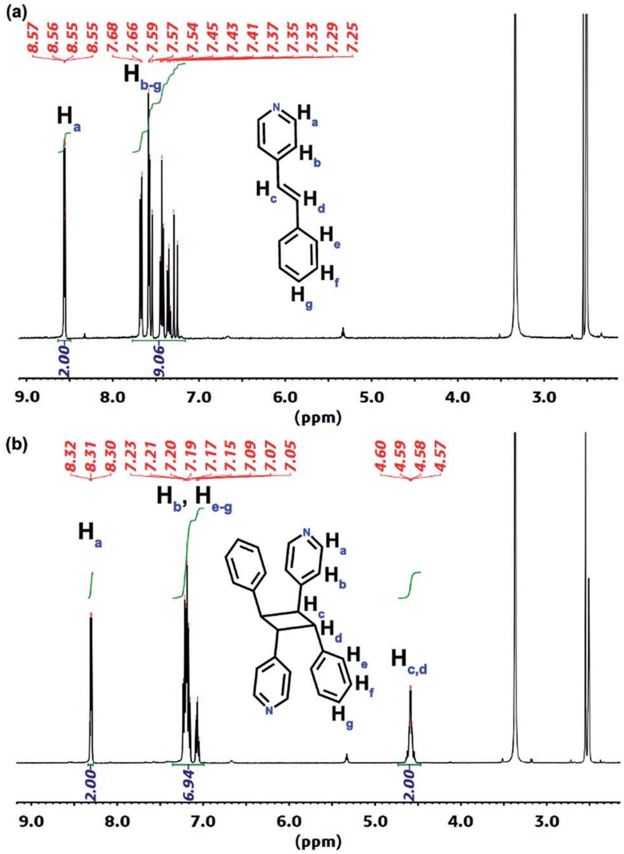

Fig. 5 ^1H NMR spectra of the framework digestion products of **1** (a) and **1′** (b).

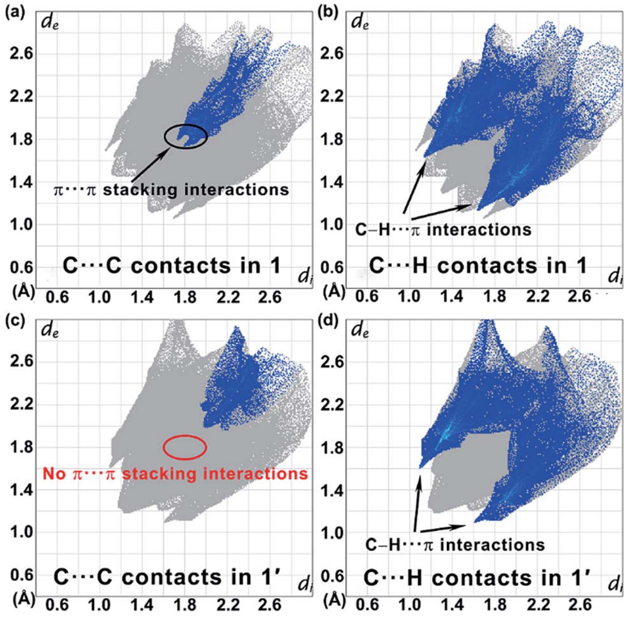

Fig. 6 The 2D fingerprint plots of C⋯C contacts (a, c) and C⋯H contacts (b, d) for **1** (a, b) and its photoproduct **1′** (c, d).

a hysteretic loop is observed (Fig. 1b), which is dramatically different from the complete, abrupt, and two-step SCO with a hysteretic loop in **2**. Therefore, not only the spin transition temperatures but also the character of the SCO can be effectively adjusted by the photochemical [2 + 2] cycloaddition reaction.

The average Fe–N distances of **1′** and **2′** at different temperatures are consistent with their magnetic states. Furthermore, the variation in the unit cell parameters of **1′** and **2′** are consistent with the magnetic curves (Fig. S20–S23†). Thus, the different SCO properties after the cycloaddition reaction are intrinsic to the electronic and structural properties of the materials rather than to the crystal lattice defects.[52] At first glance, the T_c values of **1′** are shifted to lower temperatures. By considering the structural aspect, **1′** possesses the longer Fe–N_{av} distance (2.181 Å) and smaller Fe–N–C angle (164.4°) at 260 K than those in 1 (2.157 Å and 165.4°, Table S5†), which provide a smaller ligand field and tend to decrease the $T_{1/2}$ value. By considering the electronic aspect, the π-accepting ability is decreased in **1′** when changing from an ethylene group to a cyclobutane ring, which results in a reduced ligand field to decrease the $T_{1/2}$ value. Therefore, both the structural and electronic effects support the lower spin transition temperature in **1′**. Meanwhile, the contribution to the SCO cooperativity from weaker π⋯π interactions after the cycloaddition reaction (Fig. 6 and Table S6†) outcompetes the formation of the flexible linker and results in the gradual SCO in **1′**.[24,53]

For **2** → **2′**, the average Fe–N distance decrease from 2.174 Å (185 K) to 2.145 Å (300 K) in the HS state, which hint a higher $T_{1/2}$ value in **2′**. Moreover, the breaking of the Ag–N_{py} bond after the cycloaddition reaction results in a more regular rhombic $[Fe_4\{Ag(CN)_2\}_4]$ grid (Fig. 3a–c). The Fe–N–C and C–Ag–C angles change from 164.7° and 158.2° in **2** at 185 K (HS state) to 168.8° and 175.9° in **2′** at 300 K (HS state) (Table S7†), respectively, which tend to increase the $T_{1/2}$ value. However, the decreased π-accepting ability in **2′** when changing from an ethylene group to a cyclobutane ring results in a weaker ligand field and tend to decrease the $T_{1/2}$ value. Therefore, competition between the electronic and structural effects results in the small change of $T_{1/2}$ from 155 K (**2**) to 162 K (**2′**). As for the SCO cooperativity, the contribution from weaker π⋯π interactions outcompetes the formation of the flexible linker after the cycloaddition reaction. Moreover, the loss of the Ag–N_{py} bond also decreases the SCO cooperativity for **2** → **2′**. Therefore, only an incomplete and gradual SCO behavior is observed in **2′**.

Conclusions

In summary, for the first time, we successfully integrate photochemical [2 + 2] cycloaddition reaction into the SCO magnetic systems. After UV irradiation, a SCSC transformation from 2D interdigitated layers to a 3D interpenetrated structure is achieved in **1** → **1′**. Meanwhile, a 3D → 3D photochemical transformation associated with Ag–N_{py} bonds breaking during the conversion from **2** to **2′** is firstly observed. Moreover, it is found the spin transition temperatures and characters, such as abruptness, hysteresis and steps, were obviously changed due to a series of structural and electronic perturbations caused by the dimerization reaction of photoreactive ligand, demonstrating the effective modulation of SCO behaviors. This work develops a new photochemical modulation mechanism for spin crossover materials by the [2 + 2] cycloaddition reaction, with high quantum efficiency, stable photoproducts and intact crystallinity. Such strategy not only extends the potential application of photochemical reactions in multifunction materials but also open up a new area in the designing of photo-responsive magnetic materials. Further work focused on improving performance, *e.g.* response speed and reversibility, of such photo-responsive SCO materials is on progress.

Experimental

Materials and methods

All the reagents were commercially available and used as received. The solid UV-visible absorption data were collected in the range of 4000–400 nm on a Shimadzu UV-3600Plus UV/VIS/NIR spectrometer. The FT-IR spectra were recorded in KBr tablets in the range of 4000–400 cm^{-1} on a Thermo Nicolet AVATAR 330 FT-IR spectrometer. The powder XRD patterns were recorded on a Rigaku Smartlab X-ray diffractometer with $Cu_{K\alpha}$ ($\lambda = 1.54178$ Å) radiation. Thermogravimetric (TG) analyses were performed on a PerkinElmer TGA7 thermogravimetric analyzer in a N_2 flow with a heating rate of 10 K min^{-1} from ambient temperature to 800 °C, with an empty Al_2O_3 crucible as reference. The C, H, and N microanalyses were performed for the dry crystals on an Elementar Vario-ELCHNS elemental analyzer. Differential Scanning Calorimetry (DSC) measurement was performed by cooling and heating the microcrystals sample in an aluminium crucible using a NETZSCH5, which was carried out at sweeping rate of 10 K min^{-1} under nitrogen. The ^{1}H NMR spectra were recorded at ambient temperature on a Bruker advance III HD 400 spectrometer. ^{1}H NMR chemical shifts were referenced to the solvent signal in DMSO-d_6. The UV-irradiation experiments were conducted with a high-pressure mercury lamp with $P = 500$ W. Magnetic susceptibility measurements for the microcrystals samples (20–30 mg) were performed on a Quantum Design PPMS instrument operating in the range of 5–300 K and under a field of 1000 Oe. Diamagnetic correction was performed based on the Pascal's coefficients.

^{1}H NMR experiments

For the ^{1}H NMR spectra measurement, the organic ligands in compounds **1**, **2** and their photoproducts are extracted through a reported framework digestion approach[36] with slight difference.

20 mg samples were digested in 2 mL DMSO overnight to give a dark orange solution. The solution was layered onto CH_2Cl_2 (10 mL) and then washed with H_2O for more than 5 times. The organic phase was separated and evaporated to give the solid, which was taken up in DMSO-d_6 for analysis.

Synthesis

[Fe(4-spy)$_2${Ag(CN)$_2$}$_2$] (**1**) was prepared through a vial-in-vial slow diffusion technique. A solution of $Fe(ClO_4)_2\cdot 6H_2O$ (0.05 mmol, 13 mg) in EtOH (1 mL) was placed in a 2 ml vial and a mixture of spy (0.1 mmol, 18 mg) and $KAg(CN)_2$ (0.1 mmol, 20 mg) in EtOH (1 mL) were placed in a 15 ml vial. The small vial was placed in the large one and then both of them were slowly filled with ethanol. Orange block crystals were collected after about two weeks. Yield: 63%. Anal. calcd for $C_{30}H_{22}Ag_2FeN_6$: C, 48.82; H, 3.00; N, 11.39. Found: C, 48.73; H, 3.11; N, 11.42.

[Fe(2,4-bpe)$_2${Ag(CN)$_2$}$_2$] (**2**) was prepared in the same way as described in **1** except that 4-spy ligand was replaced by the 2,4-bpe ligand. Orange block crystals were collected after about two weeks. Yield: 76%. Anal. calcd for $C_{28}H_{20}Ag_2FeN_8$: C, 45.44; H, 2.72; N, 15.14. Found: C, 45.36; H, 2.78; N, 15.04.

[Fe(*rctt*-4-ppcb){Ag(CN)$_2$}$_2$] (**1′**) was obtained through the UV irradiation of **1** for 3 days under a high-pressure mercury lamp with $P = 500$ W, which was further confirmed by the SC-XRD structural analyses, PXRD patterns, IR spectra and ^{1}H NMR spectra measurements. Anal. calcd for $C_{30}H_{22}Ag_2FeN_6$: C, 48.82; H, 3.00; N, 11.39. Found: C, 48.67; H, 2.93; N, 11.43.

[Fe(*rctt*-2,4-tpcb-ht){Ag(CN)$_2$}$_2$] (**2′**) was obtained through the UV irradiation of **2** for 4 days under a high-pressure mercury lamp with $P = 500$ W, which was further confirmed by the SC-XRD structural analyses, PXRD patterns, IR spectra and ^{1}H NMR spectra measurements. Anal. calcd for $C_{28}H_{20}Ag_2FeN_8$: C, 45.44; H, 2.72; N, 15.14. Found: C, 45.56; H, 2.81; N, 15.22.

X-ray crystallography

Single-crystal diffraction data were recorded on a Bruker D8 QUEST diffractometer with $Mo_{K\alpha}$ ($\lambda = 0.71073$ Å) radiation in sequence at 260 K, 212 K, 120 K for **1**, 260 K, 178 K, 120 K for **1′** and 300 K, 185 K, 90 K for **2′**. Single-crystal diffraction data of **2** were recorded on a Rigaku XtaLAB Synergy R diffractometer with $Cu_{K\alpha}$ ($\lambda = 1.54178$ Å) radiation in sequence at 185 K, 155 K and 120 K. The crystal structures were solved by direct methods, and all non-hydrogen atoms were refined anisotropically by least-squares on F^2 using the SHELXTL 2014/7 program.[54] Hydrogen atoms on organic ligands were generated by the riding mode. The responses to the alerts from checkCIF are quoted within the validation response form. CCDC 1897816 (260 K), 1897817 (212 K), 1897818 (120 K), for **1**, 1897822 (260 K), 1897823 (178 K), 1897824 (120 K), for **1′**, 1897819 (185 K), 1897820 (155 K), 1897821 (120 K) for **2** and 1897825 (300 K), 1897826 (185 K), 1897827 (90 K) for **2′** contain the supplementary crystallographic data for this paper.†

Conflicts of interest

There are no conflicts to declare.

Acknowledgements

This work was supported by the National Key Research and Development Program of China (2018YFA0306001), the NSFC (21773316, 21801258, 21821003, and 21771200), and the Pearl River Talent Plan of Guangdong (2017BT01C161).

Notes and references

1 O. Sato, *Nat. Chem.*, 2016, **8**, 644–656.

2 S. M. Cohen, *Chem. Sci.*, 2010, **1**, 32–36.

3 Z. Wang and S. M. Cohen, *Chem. Soc. Rev.*, 2009, **38**, 1315–1329.

4 S. M. Cohen, *Chem. Rev.*, 2012, **112**, 970–1000.

5 P. Deria, J. E. Mondloch, O. Karagiaridi, W. Bury, J. T. Hupp and O. K. Farha, *Chem. Soc. Rev.*, 2014, **43**, 5896–5912.

6 I. G. Georgiev and L. R. MacGillivray, *Chem. Soc. Rev.*, 2007, **36**, 1239–1248.

7 M. Nagarathinam, A. M. P. Peedikakkal and J. J. Vittal, *Chem. Commun.*, 2008, 5277–5288.

8 R. Medishetty, I.-H. Park, S. S. Lee and J. J. Vittal, *Chem. Commun.*, 2016, **52**, 3989–4001.

9 Y.-C. Ou, D.-S. Zhi, W.-T. Liu, Z.-P. Ni and M.-L. Tong, *Chem.–Eur. J.*, 2012, **18**, 7357–7361.

10 Y.-C. Ou, W.-T. Liu, J.-Y. Li, G.-G. Zhang, J. Wang and M.-L. Tong, *Chem. Commun.*, 2011, **47**, 9384–9386.

11 F.-L. Hu, Y. Mi, C. Zhu, B. F. Abrahams, P. Braunstein and J.-P. Lang, *Angew. Chem., Int. Ed.*, 2018, **57**, 12696–12701.

12 M. D. Cohen, G. M. J. Schmidt and F. I. Sonntag, *J. Chem. Soc.*, 1964, 2000–2013.

13 G. M. J. Schmidt, *Pure Appl. Chem.*, 1971, **27**, 647–678.

14 A. Chanthapally, G. K. Kole, K. Qian, G. K. Tan, S. Gao and J. J. Vittal, *Chem.–Eur. J.*, 2012, **18**, 7869–7877.

15 A. Hazra, S. Bonakala, K. K. Bejagam, S. Balasubramanian and T. K. Maji, *Chem.–Eur. J.*, 2016, **22**, 7792–7799.

16 L.-F. Wang, J.-Z. Qiu, J.-L. Liu, Y.-C. Chen, J.-H. Jia, J. Jover, E. Ruiz and M.-L. Tong, *Chem. Commun.*, 2015, **51**, 15358–15361.

17 L.-F. Wang, J.-Z. Qiu, Y.-C. Chen, J.-L. Liu, Q.-W. Li, J.-H. Jia and M.-L. Tong, *Inorg. Chem. Front.*, 2017, **4**, 1311–1318.

18 G. S. Papaefstathiou, Z. Zhong, L. Geng and L. R. MacGillivray, *J. Am. Chem. Soc.*, 2004, **126**, 9158–9159.

19 K. M. Hutchins, T. P. Rupasinghe, L. R. Ditzler, D. C. Swenson, J. R. G. Sander, J. Baltrusaitis, A. V. Tivanski and L. R. MacGillivray, *J. Am. Chem. Soc.*, 2014, **136**, 6778–6781.

20 B. Dutta, A. Dey, C. Sinha, P. P. Ray and M. H. Mir, *Inorg. Chem.*, 2018, **57**, 8029–8032.

21 P. Gütlich, Y. Garciaa and H. A. Goodwin, *Chem. Soc. Rev.*, 2000, **29**, 419–427.

22 E. Konig, G. Ritter and S. K. Kulshreshtha, *Chem. Rev.*, 1985, **85**, 219–234.

23 H. Spiering, E. Meissner, H. Köppen, E. W. Müller and P. Gütlich, *Chem. Phys.*, 1982, **68**, 65–71.

24 M. A. Halcrow, *Chem. Soc. Rev.*, 2011, **40**, 4119–4142.

25 M. C. Muñoza and J. A. Real, *Coord. Chem. Rev.*, 2011, **255**, 2068–2093.

26 Z.-P. Ni, J.-L. Liu, M. N. Hoque, W. Liu, J.-Y. Li, Y.-C. Chen and M.-L. Tong, *Coord. Chem. Rev.*, 2017, **335**, 28–43.

27 W. Liu, Y.-Y. Peng, S.-G. Wu, Y.-C. Chen, M. N. Hoque, Z.-P. Ni, X.-M. Chen and M.-L. Tong, *Angew. Chem., Int. Ed.*, 2017, **56**, 14982–14986.

28 M. Ohba, K. Yoneda, G. Agustí, M. C. Muñoz, A. B. Gaspar, J. A. Real, M. Yamasaki, H. Ando, Y. Nakao, S. Sakaki and S. Kitagawa, *Angew. Chem., Int. Ed.*, 2009, **48**, 4767–4771.

29 P. D. Southon, L. Liu, E. A. Fellows, D. J. Price, G. J. Halder, K. W. Chapman, B. Moubaraki, K. S. Murray, J.-F. Létard and C. J. Kepert, *J. Am. Chem. Soc.*, 2009, **131**, 10998–11009.

30 E. Coronado, M. Giménez-Marqus, G. M. Espallargas, F. Rey and I. J. Vitórica-Yrezábal, *J. Am. Chem. Soc.*, 2013, **135**, 15986–15989.

31 G. J. Halder, C. J. Kepert, B. Moubaraki, K. S. Murray and J. D. Cashion, *Science*, 2002, **298**, 1762–1765.

32 J.-Y. Ge, Z. Chen, L. Zhang, X. Liang, J. Su, M. Kurmoo and J.-L. Zuo, *Angew. Chem., Int. Ed.*, 2019, **58**, 8789–8793.

33 X. Bao, H. J. Shepherd, L. Salmon, G. Molnar, M. L. Tong and A. Bousseksou, *Angew. Chem., Int. Ed.*, 2013, **52**, 1198–1202.

34 G. Agustí, R. Ohtani, K. Yoneda, A. B. Gaspar, M. Ohba, J. F. Sánchez-Royo, M. C. Muñoz, S. Kitagawa and J. A. Real, *Angew. Chem., Int. Ed.*, 2009, **48**, 8944–8947.

35 R. Ohtani, K. Yoneda, S. Furukawa, N. Horike, S. Kitagawa, A. B. Gaspar, M. C. Muñoz, J. A. Real and M. Ohba, *J. Am. Chem. Soc.*, 2011, **133**, 8600–8605.

36 J. E. Clements, J. R. Price, S. M. Neville and C. J. Kepert, *Angew. Chem., Int. Ed.*, 2014, **53**, 10164–10168.

37 M. M. Khusniyarov, *Chem.–Eur. J.*, 2016, **22**, 15178–15191.

38 B. Brachňaková and I. Šalitroš, *Chem. Pap.*, 2018, **72**, 773–798.

39 M.-L. Boillot, C. Roux, J.-P. Audière, A. Dausse and J. Zarembowitch, *Inorg. Chem.*, 1996, **35**, 3975–3980.

40 M.-L. Boillot, S. Pillet, A. Tissot, E. Rivière, N. Claiser and C. Lecomte, *Inorg. Chem.*, 2009, **48**, 4729–4736.

41 Y. Hasegawa, K. Takahashi, S. Kume and H. Nishihara, *Chem. Commun.*, 2011, **47**, 6846–6848.

42 Y. Hasegawa, S. Kume and H. Nishihar, *Dalton Trans.*, 2009, 280–284.

43 B. Rçsner, M. Milek, A. Witt, B. Gobaut, P. Torelli, R. H. Fink and M. M. Khusniyarov, *Angew. Chem., Int. Ed.*, 2015, **54**, 12976–12980.

44 M. Estrader, J. S. Uber, L. A. Barrios, J. Garcia, P. Lloyd-Williams, O. Roubeau, S. J. Teat and G. A. Aromí, *Angew. Chem., Int. Ed.*, 2017, **56**, 15622–15627.

45 M. Nihei, Y. Suzuki, N. Kimura, Y. Kera and H. Oshio, *Chem.–Eur. J.*, 2013, **19**, 6946–6949.

46 Z.-Y. Li, J.-W. Dai, M. Damjanović, T. Shiga, J.-H. Wang, J. Zhao, H. Oshio, M. Yamashita and X.-H. Bu, *Angew. Chem., Int. Ed.*, 2019, **58**, 4339–4344.

47 V. A. Blatov, *Struct. Chem.*, 2012, **23**, 955–963.

48 E. V. Alexandrov, V. A. Blatov, A. V. Kochetkova and D. M. Proserpio, *CrystEngComm*, 2011, **13**, 3947–3958.

49 G. Agustí, A. B. Gaspar, M. C. Muñoz, P. G. Lacroix and J. A. Real, *Aust. J. Chem.*, 2009, **62**, 1155–1165.

50 M. J. Turner, J. J. McKinnon, S. K. Wolff, D. J. Grimwood, P. R. Spackman, D. Jayatilaka and M. A. Spackman, *Crystal Explorer 17*, University of Western Australia, 2017.

51 J. J. McKinnon, M. A. Spackmana and A. S. Mitchell, *Acta Crystallogr., Sect. B: Struct. Sci.*, 2004, **60**, 627–668.

52 M. S. Haddad, W. D. Federer, M. W. Lynch and D. N. Hendrickson, *Inorg. Chem.*, 1981, **20**, 131–139.

53 J. A. Real, A. B. Gaspar, V. Niel and M. C. Muñoz, *Coord. Chem. Rev.*, 2003, **236**, 121–141.

54 G. M. Sheldrick, *Acta Crystallogr., Sect. A: Found. Crystallogr.*, 2008, **64**, 112–122.